Observation of Fluctuation Spin Hall Effect in Antiferromagnet

Chi Fang[†1,2], Caihua Wan[†1,7], Xiaoyue Zhang[3,5], Satoshi Okamoto[4], Tianyi Ma[1,3],

Jianying Qin[1,3], Xiao Wang[1], Chenyang Guo[1], Jing Dong[1], Guoqiang Yu[1,7], Zhenchao

Wen[6], Ning Tang[5], Stuart S. P. Parkin[2], Naoto Nagaosa[9] , Yuan Lu[3*], Xiufeng Han[1,7,8*]

[1]*Beijing National Laboratory for Condensed Matter Physics, Institute of Physics,*

University of Chinese Academy of Sciences, Chinese Academy of Sciences, Beijing

100190, China

[2]*Max Planck Institute of Microstructure Physics, Halle (Saale) 06120, Germany*

[3]*Université de Lorraine, CNRS, Institut Jean Lamour, UMR 7198, campus ARTEM, 2*

Allée André Guinier, 54011 Nancy, France

[4]*Materials Science and Technology Division, Oak Ridge National Laboratory, Oak*

Ridge, TN 37831, USA

[5]*State Key Laboratory of Artificial Microstructure and Mesoscopic Physics, School of*

Physics, Peking University, Beijing 100871, China

[6]*National Institute for Materials Science NIMS, Tsukuba, Ibaraki 3050047, Japan*

[7]*Songshan Lake Materials Laboratory, Dongguan, Guangdong 523808, China*

[8]*Center of Materials Science and Optoelectronics Engineering, University of Chinese*

Academy of Sciences, Beijing 100049, China

[9]*RIKEN Center for Emergent Matter Science (CEMS), Wako, 351-0198, Japan.*

†These two authors contributed equally to this work.

*Corresponding Authors: yuan.lu@univ-lorraine.fr, xfhan@iphy.ac.cn,

Abstract

The spin Hall effect (SHE) can generate a pure spin current by an electric current, which is promisingly used to electrically control magnetization. To reduce power consumption of this control, a giant spin Hall angle (SHA) in the SHE is desired in low-resistivity systems for practical applications. Here, critical spin fluctuation near the antiferromagnetic (AFM) phase-transition is proved as an effective mechanism to create an additional part of SHE, named as fluctuation spin Hall effect (FSHE). This FSHE enhances the SHA due to the AFM spin fluctuation between conduction electrons and local spins. We detect the FSHE with the inverse and direct spin Hall effect (ISHE and DSHE) set-up and their temperature (T) dependences in the Cr/MgO/Fe magnetic tunnel junctions (MTJs). The SHA is significantly enhanced when temperature is approached to the Néel temperature (T_N) and has a peak value of -0.34 at 200 K near T_N. This value is higher than the room-temperature value by 240% and comparable to that of heavy metals Ta and W. Furthermore, the spin Hall resistivity of Cr well fits the modeled T-dependence when T approaches T_N from low temperatures, implying the AFM spin fluctuation nature of strong SHA enhancement. Thus, this study demonstrates the critical spin fluctuation as a prospective way of increasing SHA and enriches the AFM material candidates for spin-orbitronic devices.

The spin Hall effect utilizes spin-orbit coupling to convert a longitudinal charge current j_c into a transverse pure spin current j_s. j_s at the interface can be further absorbed by a magnetic thin film, exert a spin-orbit torque (SOT) on the magnet and finally drive its

switching or oscillation. Owing to the electrical controllability on magnetization, the SHE shows promising applications in magnetic random-access memory (MRAM)[1-3], programmable logic devices[4,5] and microwave nano-oscillators[6].

SHA (θ_{SH}) defined as the ratio between j_s and j_c, or alternatively, the ratio between spin Hall conductivity σ_{SH} and longitudinal conductivity σ. Companied by the factor of high σ, θ_{SH} is the key factor to reduce writing power and achieve high efficiency of SOT devices[7]. Thus, it is appealing to develop materials and/or explore physics to improve θ_{SH} in low-resistive systems[8,9].

The microscopic mechanisms behind the SHE have been extensively investigated. They can be categorized into three pictures, the intrinsic one due to the nontrivial Berry curvatures of electronic band structures and the other two extrinsic ones, the side-jump(sj) and skew-scattering(ss) mechanisms[8]. Inspired by the mechanisms, several effective means have been developed to enhance the SHA, such as electronic structure engineering[10], doping[11], interface decoration[12] and superlattice stacking[13]. For example, because of the intrinsic mechanism, the heavy metals Ta[14,15], Pt[16-18], W[19] with large atomic numbers[18] or some topological insulators with symmetry-protected surface states[20,21] are found to own large θ_{SH}. The extrinsic mechanisms are taken into account when the spin-orbit-coupling (SOC) related scatterings between delocalized electrons and local spins are considered. It is reported that doping heavy-metal dopants into a small-SHA matrix or reverse could remarkably enhance θ_{SH} of the matrix material, such as Ir-doped Cu[22] and Pt-doped Au[7].

Significantly different from the SHE in normal metals, the FSHE contribution we

reported here only involves the two extrinsic mechanisms excluding the intrinsic one since thermally-activated fluctuation of spin lattice can only contribute to the former, which can be deemed as an evidence to show the impact of the extrinsic mechanism to the overall SHE. Recently, critical spin fluctuation in magnetically-ordered systems at their magnetic phase transition temperatures T_C was reported to nontrivially result in an elevated θ_{SH} by intensifying interaction of delocalized electrons with local spins. For ferromagnets, Wei et al.[23] found an ISHE anomaly near T_C in the weak ferromagnet NiPd alloys. Ou et al.[24] observed an enhanced $\theta_{SH} \sim 0.34$ in the Fe_xPt_{1-x} alloy at its T_C. Wu et al.[25] observed a $\theta_{SH} \sim 0.46$ in Ni_xCu_{1-x} alloys due to spin fluctuation around T_C. For antiferromagnets, Saglam et al.[26] evidenced that spin fluctuation of the antiferromagnetic FeMn at its Néel temperature increased θ_{SH} of the $Ni_{80}Fe_{20}$/FeMn/W trilayer in a spin-pumping experiment. These ferromagnetic and antiferromagnetic systems have clearly hinted the contribution of spin fluctuations to the enhanced SHE phenomenally; however, all the above systems contain interfaces with ferromagnetic films, which are still too complex to purify the bulk SHE from possibly entangled interfacial effects such as the spin mixing conductance, spin memory loss and magnetic proximity effects. An elaborately designed AFM system without any ferromagnetic(FM)/AFM interfaces can promisingly provide a clearer platform to investigate the influence of spin fluctuations on the bulk SHE.

Among antiferromagnets, polycrystalline Cr has already shown sizable θ_{SH} from -0.051[27] to -0.09[28, 29] and low resistivity as a candidate SOT source. Here, we furthermore choose the epitaxial Cr single crystalline films sandwiched by MgO as the

AFM material to uncover the influence of spin fluctuations on the SHE near its T_N. To target the goal, specifically, we measured the spin Hall tunneling spectroscopy (SHTS) for the Cr/MgO/Fe fully epitaxial magnetic tunnel junctions (MTJs) which ideally have no direct FM/AFM interface as desired. In this work, we demonstrated a large θ_{SH} of -0.34 at T=200 K by measuring the SHTS for the Cr/MgO/Fe MTJs. The temperature dependence of θ_{SH} clearly showed an enhancement by 240% near T_N=206 K than at 300 K. Furthermore, the spin Hall resistivity followed a clear power law with T in consistent with modeled ones. All these results demonstrate the antiferromagnetic spin fluctuation mechanism offers an effective way indeed to enhance the bulk SHE as T approaching T_N.

AFM Spin Fluctuation

Another uniqueness of the FSHE is as following: it is attributed to the combinations of several individual scattering processes between conduction electrons and local spins as explained below, instead of a single process accounting for the SHE. These involved local spins are needed to stay correlated within a certain correlation length, which thus makes the FSHE process temperature-sensitive. In theory, taking spin fluctuation near the Curie temperature (T_C) into account, Kondo first developed a theory to explain the anomalous Hall effect in ferromagnets[30]. It is further generalized to account for the SHE and ISHE by considering the short-range spin-spin interaction[31] and the long-range dynamical correlation among localized moments[32]. Okamoto *et al.*[32] derived spin Hall conductivity σ_{SH}^{sj} and σ_{SH}^{ss} due to the extrinsic side-jump and skew-scattering mechanisms, respectively, based on the Kondo's Model, which predicts the nontrivial

SHA enhancement around the ferromagneic quantum critical point due to the critical spin fluctuations. For the AFM spin fluctuation, while the individual scattering processes $\mathcal{F}_{0,1}$, $\mathcal{F}_2$ and $\mathcal{F}_3$ (defined in Ref. 32 and schematically shown in Fig. 1) remain the same as the ferromagnetic case, the microscopic mechanisms of the side-jump and skew-scattering contributions (Fig.1b) to the SHE by the AFM spin fluctuation require further developments (as shown in Methods). Schematically, the microscopic details of the side-jump and skew-scattering mechanisms (Fig.1b) consist of three scattering processes: the $\mathcal{F}_{0,1}$ process contributes 180º back-scattering of antiparallelly polarized conduction electrons (yellow arrow) with local spins (green arrow); the $\mathcal{F}_2$ and $\mathcal{F}_3$ processes result in transverse scattering of electrons depending on the polarization of local spins and scattered electron spins, respectively[32]. Thus, the sequential scattering due to the $\mathcal{F}_{0,1}$ and $\mathcal{F}_2$ ($\mathcal{F}_3$) processes gives rise to the transverse spin current, leading to the side-jump (skew-scattering) mechanism. Temperature is involved in these extrinsic SHE processes by two ways: (1) the more dynamical spins, functioning as the local scattering centers, are activated with the increase in T toward the ordering temperature as shown in Fig. 1a, and (2) the correlation length ξ between the dynamically-activated local spins increases as T approaches the ordering temperature from above, both of which favors the sequential happening of the $\mathcal{F}_{0,1}$ and $\mathcal{F}_2$ ($\mathcal{F}_3$) processes in a higher probability. Moreover, there is no limitation for the above microscopic processes to take place above or below the ordering temperature, in contrast to ferromagnetically ordered systems where the pure SHE is expected to exist only above the transition temperature because below the

transition temperature the anomalous Hall effect appears. Therefore, the AFM order is necessary to observe a pure spin-fluctuation-originated contribution to the SHE, i.e., FSHE, without involvement with the anomalous Hall effect. Specifically, one would then expect a clear enhancement of the SHE in an antiferromagnetic system around its Néel temperature at which the correlation length diverges. This hypothesis motivated us to experimentally study the influence of AFM spin fluctuations on the bulk SHE in the clean Cr/MgO/Fe MTJs by the clear SHTS method, which is also instructive to develop the correspondingly theories.

Single Crystal Cr Junction

Chromium is a typical antiferromagnet with collinear spin sublattices and a simple body-centered cubic (bcc) structure. T_N of bulk Cr is 311 K and lowerable by reducing thickness. Epitaxial stacks Cr(t)/MgO(2.3)/Fe(10)/Au(5 nm) (t =7, 10, 25, 50 nm) was deposited on a MgO (001) substrate by the molecular beam epitaxial growth(Methods). Note that Cr in these MTJs were spaced by MgO from Fe, which avoided direct Cr/Fe interfaces and ideally disentangled the targeted bulk Cr SHE from any interfacial spin-mixing, spin memory loss or magnetic proximity effects[33, 34].

The Fe layer was used as a spin-polarizer of charge current and the Cr layer functioned as a spin-analyzer to convert a spin current into a transverse voltage via the ISHE. The high-resolution cross-sectional transmission electron microscope (HRXTEM) was used to check the MTJ structure (Fig. 2a). The low-mag image validated uniform thickness for each layer well corresponding to the nominal one. The black field image (inset of Fig. 2a) allows us to measure the lattice constant of each layer. The lattice constants of

the bcc Cr and Fe near interfaces were a_{Cr}=2.91 Å and a_{Fe}=2.88 Å, close to their bulk

values 2.88 Å and 2.87 Å [35]. A_{MgO}=4.24 Å [36] was near $\sqrt{2}\,a_{Cr}$=4.11 Å and

$\sqrt{2}\,a_{Fe}$=4.06 Å, which implied the epitaxial relationship: $(001)_{MgO}//(001)_{Cr/Fe}$ and

$[100]_{MgO}//[110]_{Cr/Fe}$[36]. The electron energy loss spectroscopy (EELS) was performed to

map the elementary distributions (Fig. 2b). There was negligible interdiffusion for the

Cr, Fe, Mg and Au elements between neighboring layers. Fig. 2c and its inset show the

magnetic hysteresis loops as the magnetic field **H** applied along the in-plane $[110]_{MgO}$,

$[100]_{MgO}$ and out-of-plane $[001]_{MgO}$ directions by vibrating sample magnetometer

(VSM). The loops verified the in-plane easy axis indeed along the $[110]_{MgO}$ direction.

This epitaxial relation attributed to the born magnetic easy-axis of Fe and the AFM

ordering of Cr along the $[110]_{MgO}$ direction owing to the magnetocrystalline anisotropy.

A single 10-nm Cr was deposited on MgO (001) as a control sample and fabricated into

the 4-Probe Bar to determine the T_N of Cr. As shown in Fig. 2d, the resistivity ρ gained

an extra enhancement due to the disorder-induced scattering via spin fluctuation near

T_N[36, 37]. The differential resistivity ρ respective to T, i.e., (dρ/dT) captured this

enhancement clearly. As T>206 K, $d\rho/dT$ maintained stable platform with a small

slope. From 206 K to lower T, $d\rho/dT$ began to acquire an extra slope because spin

fluctuation scattering was switched on in this case. With further lowering T and freezing

the AFM structure, after a peak at 150 K, $d\rho/dT$ finally approached to a smaller but

stable value due to the decrease in magnon density. This behavior, similar with Ref. 37,

indicated T_N of Cr was ~206 K. This value is near T_N=235 K of the epitaxial 50 nm Cr

as reported[37].

Spin Hall Tunneling Spectroscopy

To investigate the SHE in Cr, the SHTS and the harmonic lock-in setup[33, 34] were adopted. The raw film was fabricated into 6×6 μm^2 MTJs with one top electrode and three bottom ones (Fig. 3a). For detecting the ISHE, an ac current J was injected between Electrodes 1 and 3 (Fig. 3b inset). The magnetization M_{Fe} stayed along MgO [110]. Thus the injected current was spin-polarized along [110] before electrons tunneled through the MgO barrier and entered into Cr. SHE in Cr led to the transverse scattering of the tunneling spin current along the MgO [-110] direction so that an electric field between Electrode 2 and 4 was built as $V_{ISHE} \propto \theta_{SH}(\mathbf{j}_s \times \mathbf{s})$. $\mathbf{j}_s(\mathbf{s})$ indicates the flowing direction of the spin current along the film normal (spin-polarized direction determined by the magnetization of Fe, i.e., $\mathbf{M}_{Fe}$). Then, one could control the output voltage V_{ISHE} or resistance (dV_{ISHE}/dJ) by $\mathbf{M}_{Fe}$ with an external field $\mathbf{H}$. When $\mathbf{H}$ is applied out-of-plane along the film normal, dV_{ISHE}/dJ vanishes because of the zero $(\mathbf{j}_s \times \mathbf{s})$ term (Methods). When $\mathbf{H}$ was in-plane and parallel or antiparallel to $[110]_{MgO}$, $(\mathbf{j}_s \times \mathbf{s})$ as well as (dV_{ISHE}/dJ) reached its positive or negative maximum. The maximized $|dV_{ISHE}/dJ|$ value was defined as R_{ISHE}. When the $\mathbf{H}$ direction fixed, R_{ISHE} measured in Cr had the same (opposite) sign as in Ta (Pt), indicating Cr shared the same θ_{SH} sign with Ta. This observation accorded with the previous reports[27, 28, 33]. Besides, we also measured SHTS with increasing J from 10 μA to 70 μA. The magnitude of R_{ISHE} keeps nearly the same as expected (Methods).

Temperature Dependence

To observe the critical spin fluctuation enhancement, we performed the SHTS

measurement at different T from 50 K to 300 K with an interval of 25 K. The extracted R_{ISHE} values were plotted in Fig. 3c. Below the critical point 206 K, R_{ISHE} increased rapidly as elevating T. Above 206 K, R_{ISHE} was reduced as increasing T further. T_{max} where R_{ISHE} was maximized was almost identical to T_N. This enhancement behavior in the temperature dependence is also observed in other samples (Extended Data Fig. 4). To eliminate any possible contributions from the spin transport artifacts in Fe, we also adopted the direct spin Hall effect (DSHE)[34] setup for the same device (Fig. 3b lower panel). In the DSHE measurement, a current was applied between Electrode 2 and 4, which produced a spin accumulation at the Cr/MgO interface. A DSHE voltage V_{DSHE} was then detected by the Fe electrode because of the spin accumulation at the Cr/MgO interface. The magnitude of V_{DSHE} is then proportional to $\mathbf{M}_{Fe}$[38, 39]. V_{DSHE} and thus $R_{DSHE} = (dV_{DSHE}/dJ)_{max}$ across the MTJ was collected between Electrode 1 and 3 to evaluate the SHE (Fig. 3b inset). In this setup, no current flowed through the Fe layer, so V_{DSHE} had no chances to be involved with any magnetotransport artifacts in Fe. The T-dependence of R_{DSHE} also showed an enhancement around 200 K, coinciding with the ISHE result. Both T-dependence indicated an enhancement of SHE near T_N of Cr, which was attributed to the enhanced fluctuation of local spins near T_N as quantitively analyzed below.

For the same spin polarizer and setup, (dV_{ISHE}/dJ) depends on intrinsic properties of the spin analyzer material, which enables the SHTS to characterize spin Hall materials[26]. To qualify the enhancement, we calculated θ_{SH} at different T. θ_{SH} can be deduced from Equation (1) given by Liu et al.[34].

$$R_{ISHE} = \left(\frac{dV_{ISHE}}{dJ}\right)_{max} = \frac{\theta_{SH}P\rho}{w} \cdot \frac{\lambda_s}{t} \cdot tanh(t/2\lambda_s) \tag{1}$$

where P denotes the spin polarization of FM layer, λ_s is the spin diffusion length of Cr, t and w is the thickness and channel width of Cr layer, respectively. Thus, given the R_{ISHE} values and other parameters, one can estimate θ_{SH} of the Cr layer. To estimate θ_{SH}, λ_s is necessary. As the reported λ_s varies dramatically from 2.1 nm to 13.3 nm[27, 28, 40] in literatures, we determined the λ_s in our own MTJs with different Cr thicknesses as shown in Fig. 4a. Reforming Equation (1), Equation (2) containing λ_s as a fitting parameter could be derived.

$$wtR_{ISHE}/(P\rho) = \theta_{SH}\lambda_s tanh(t/2\lambda_s) = A(t) \tag{2}$$

We used the parameters at 300 K to figure out λ_s=8.96±0.37 nm (Fig. 4b). Note that the reported λ_s of materials with large SHA slightly but monotonously declines[41, 42] with increasing T. This factor cannot increase the injected spin current and has no way to contribute an enhanced SHE as T was elevated from low. The enhanced R_{ISHE} and R_{DSHE} signals can be only ascribed to an enlarged SHA directly instead of the variation of λ_s. Thus we supposed a temperature-insensitive λ_s in the fitting of Fig. 4b accordingly. With this λ_s, θ_{SH} could be calculated from the equation (1). For instance, R_{ISHE} =3.13 mΩ at 200 K, P=0.74 for single crystal Fe/MgO electrode[43], w=10 μm, t=10 nm, ρ=33.89 μΩ·cm, then we have $|\theta_{SH}|$=0.34. The θ_{SH} in 10 nm Cr equals to -0.34 at 200 K and -0.10 at 300 K (Fig. 4c). The 300 K value is comparable to but higher than the literature values of -0.051 to -0.09[29], probably due to no magnetic interface influences here. Moreover, spin fluctuation near T_N caused a remarkable SHA enhancement by 240% at 200 K compared to 300 K. The 200 K value has already been

comparable to that of heavy metals[44], inferring Cr can function as an efficient SOT source. Besides, the Cr film has relatively low resistivity of about 30 μΩ·cm, nearly one order of magnitude lower than ~190 μΩ·cm of the β-phase Ta[14] and 100-300 μΩ·cm of the β-phase W[19] systems, which can further improve its energy-efficiency. These merits, the large SHA and low resistivity, persist below or around the Néel temperature, which facilitates the use of Cr as a SOT channel material in spin-orbitronics.

Discussion

To examine the mechanism of the observed SHE, the scaling relation between spin conductivity σ_{SH} and conductivity σ of Cr is plotted in Fig.4d. The scaling relation does not simply follow $\sigma_{SH} \propto constant$ for the side-jump or intrinsic mechanism or $\sigma_{SH} \propto \sigma$ for the skew-scattering mechanism. A clear transition point emerges around T_N rather than a gradual crossover behavior due to mechanism switch[45].

Equation (1) showed the main contributing factor to the enhanced R_{ISHE} was $\theta_{SH}\rho$, the spin Hall resistivity. Normally both spin polarization P [46] and the term $\frac{\lambda_s}{t} \cdot$ $\tanh(t/2\lambda_s)$ involving λ_s [41, 42] should maintain stable or decrease slightly but monotonically as T increases. Consequently, these two terms could not account for the rising R_{ISHE} before T_N. In Fig. 4e we show the T-dependence of $|\theta_{SH}\rho|$. When the skew scattering provides dominant contribution to the SHE, $|\theta_{SH}\rho|=|\sigma_{SH}/\sigma^2|$ serves as an indicator of the SOC strength suggested in Ref. 32. $|\theta_{SH}\rho|$ followed a $T^{3.65}$ power law at low $T<T_{max}$ (Extended Data Fig. 5b). It appears similar to the predicted behavior near the ferromagnetic quantum critical point with $T^{10/3}$. AFM materials could have different power laws, in particular when magnetic ordering appears at finite temperature.

Note that even though the scattering processes of $\mathcal{F}_{0,1}$ and $\mathcal{F}_2$ ($\mathcal{F}_3$) also take place in AFM materials, the way how they cooperate together to contribute to the SHE can be different from the ferromagnetic counterpart. The long-range dynamical correlation length among localized spins which determines the probability of sequential occurrence of the $\mathcal{F}_{0,1}$ and $\mathcal{F}_2$ ($\mathcal{F}_3$) processes can differ between AFM and FM materials. These factors jointly result in a different T-power law in Cr from the 10/3 value due to the ferromagnetic critical fluctuation, which can be used as a benchmark and worth further theoretical investigation. When considering AFM spin fluctuation, Kondo model could be generalized to give $\sigma_{SH}^{ss}/\sigma^2 \propto T^6$ for the skew-scattering mechanism and $\sigma_{SH}^{sj}/\sigma^2 \propto T^2 + \alpha T^4$ for the side-jump mechanism, where α is a constant deduced from the T-dependence of ρ (Methods). Both expressions could give a good fit to the experimental data, as shown in Fig. 4d, which persuades us to attribute the enhanced SHA to the AFM spin fluctuation. Although the fitting according to the side-jump mechanism gives a higher confidence, it is still hard to claim which mechanism dominates the enhancement, which will be further investigated hereafter.

Above T_N, the AFM texture of Cr is no longer stable. On the other hand, the electron-phonon and electron-electron interactions that weakly depend on spins gradually dominate the T-dependence of momentum relaxation process with a T^5 law[47, 48] and T^2 law[49], respectively. These spin-irrelevant processes contribute more to momentum-relaxation scatterings than the spin fluctuation mechanism. As a natural result, $\theta_{SH}\rho$ inclined to decrease gradually.

Conclusion

In conclusion, we investigated the spin Hall angles and its temperature dependence of Cr in Cr/MgO/Fe fully epitaxial MTJs. Critical spin fluctuation enhancement of θ_{SH} to -0.34 in Cr by 240% near T_N=206 K than 300 K was observed. The dependence of $\theta_{SH}\rho$ on T before T_N was experimentally measured and fitted with the modeled T-dependence of the AFM spin fluctuation. This effective mechanism of increasing spin Hall angles can be instructive to design antiferromagnets with much larger spin Hall angles and low resistivity, and further advance AFM applications in SOT devices.

References

1. Yu, G., Upadhyaya, P., Fan, Y., Alzate, J. G., Jiang, W., Wong, K. L., et al. Switching of perpendicular magnetization by spin-orbit torques in the absence of external magnetic fields. *Nat. Nanotechnol.* **9**(7)**,** 548(2014).
2. Fukami, S., Zhang, C., DuttaGupta, S., Kurenkov, A., Ohno, H. Magnetization switching by spin-orbit torque in an antiferromagnet-ferromagnet bilayer system. *Nat. Mater.* **15**(5)**,** 535(2016).
3. Oh, Y.-W., Baek, S.-H. C., Kim, Y. M., Lee, H. Y., Lee, K.-D., Yang, C.-G., et al. Field-free switching of perpendicular magnetization through spin-orbit torque in antiferromagnet/ferromagnet/oxide structures. *Nat. Nanotechnol.* **11**(10)**,** 878(2016).
4. Wan, C., Zhang, X., Yuan, Z., Fang, C., Kong, W., Zhang, Q., et al. Programmable Spin Logic Based on Spin Hall Effect in a Single Device. *Adv. Electron. Mater.* **3**(3)**,** 1600282(2017).
5. Wang, X., Wan, C., Kong, W., Zhang, X., Xing, Y., Fang, C., et al. Field-Free Programmable Spin Logics via Chirality-Reversible Spin-Orbit Torque Switching. *Adv. Mater.* **30**(31)**,** 1801318(2018).
6. Liu, L., Pai, C.-F., Ralph, D. C., Buhrman, R. A. Magnetic Oscillations Driven by the Spin Hall Effect in 3-Terminal Magnetic Tunnel Junction Devices. *Phys. Rev. Lett.* **109**(18)**,** 186602(2012).
7. Zhu, L., Ralph, D. C., Buhrman, R. A. Highly Efficient Spin-Current Generation by the Spin Hall Effect in Au1-xPtx. *Phys. Rev. Appl.* **10**(3)**,** 031001(2018).
8. Sinova, J., Valenzuela, S. O., Wunderlich, J., Back, C. H., Jungwirth, T. Spin Hall effects. *Rev. Mod. Phys.* **87**(4)**,** 1213(2015).
9. Hoffmann, A. Spin Hall Effects in Metals. *Ieee Transactions on Magnetics* **49**(10)**,** 5172-5193(2013).
10. Wu, H., Zhang, P., Deng, P., Lan, Q., Pan, Q., Razavi, S. A., et al. Room-Temperature Spin-Orbit Torque from Topological Surface States. *Phys. Rev. Lett.* **123**(20)**,** 207205(2019).
11. Gradhand, M., Fedorov, D. V., Zahn, P., Mertig, I. Spin Hall angle versus spin diffusion

length: Tailored by impurities. *Phys. Rev. B* **81**(24), 245109(2010).

12. Qiu, X., Narayanapillai, K., Wu, Y., Deorani, P., Yang, D.-H., Noh, W.-S., et al. Spin–orbit-torque engineering via oxygen manipulation. *Nat. Nanotechnol.* **10**(4), 333-338(2015).

13. Zhu, L., Li, J., Zhu, L., Xie, X. Boosting Spin-Orbit-Torque Efficiency in Spin-Current-Generator/Magnet/Oxide Superlattices. *Phys. Rev. Appl.* **18**(6), 064052(2022).

14. Liu, L., Pai, C.-F., Li, Y., Tseng, H. W., Ralph, D. C., Buhrman, R. A. Spin-Torque Switching with the Giant Spin Hall Effect of Tantalum. *Science* **336**(6081), 555-558(2012).

15. Gomez, J. E., Tedlla, B. Z., Alvarez, N. R., Alejandro, G., Goovaerts, E., Butera, A. Spin transport parameters in $Ni_{80}Fe_{20}$/Ru and $Ni_{80}Fe_{20}$/Ta bilayers. *Phys. Rev. B* **90**(18), 184401(2014).

16. Ando, K., Takahashi, S., Harii, K., Sasage, K., Ieda, J., Maekawa, S., et al. Electric manipulation of spin relaxation using the spin Hall effect. *Phys. Rev. Lett.* **101**(3), 036601(2008).

17. Liu, L., Moriyama, T., Ralph, D. C., Buhrman, R. A. Spin-Torque Ferromagnetic Resonance Induced by the Spin Hall Effect. *Phys. Rev. Lett.* **106**(3), 036601(2011).

18. Guo, G. Y., Murakami, S., Chen, T. W., Nagaosa, N. Intrinsic spin Hall effect in platinum: First-principles calculations. *Phys. Rev. Lett.* **100**(9), 096401(2008).

19. Pai, C.-F., Liu, L., Li, Y., Tseng, H. W., Ralph, D. C., Buhrman, R. A. Spin transfer torque devices utilizing the giant spin Hall effect of tungsten. *Appl. Phys. Lett.* **101**(12), (2012).

20. Han, J., Richardella, A., Siddiqui, S. A., Finley, J., Samarth, N., Liu, L. Room-Temperature Spin-Orbit Torque Switching Induced by a Topological Insulator. *Phys. Rev. Lett.* **119**(7), 077702(2017).

21. Mellnik, A. R., Lee, J. S., Richardella, A., Grab, J. L., Mintun, P. J., Fischer, M. H., et al. Spin-transfer torque generated by a topological insulator. *Nature* **511**(7510), 449(2014).

22. Niimi, Y., Morota, M., Wei, D. H., Deranlot, C., Basletic, M., Hamzic, A., et al. Extrinsic Spin Hall Effect Induced by Iridium Impurities in Copper. *Phys. Rev. Lett.* **106**(12), 126601(2011).

23. Wei, D. H., Niimi, Y., Gu, B., Ziman, T., Maekawa, S., Otani, Y. The spin Hall effect as a probe of nonlinear spin fluctuations. *Nat. Commun.* **3**(1), 1058(2012).

24. Ou, Y. X., Ralph, D. C., Buhrman, R. A. Strong Enhancement of the Spin Hall Effect by Spin Fluctuations near the Curie Point of FexPt1-x Alloys. *Phys. Rev. Lett.* **120**(9), 097203(2018).

25. Wu, P.-H., Qu, D., Tu, Y.-C., Lin, Y.-Z., Chien, C. L., Huang, S.-Y. Exploiting Spin Fluctuations for Enhanced Pure Spin Current. *Phys. Rev. Lett.* **128**(22), 227203(2022).

26. Saglam, H., Zhang, W., Jungfleisch, M. B., Sklenar, J., Pearson, J. E., Ketterson, J. B., et al. Spin transport through the metallic antiferromagnet FeMn. *Phys. Rev. B* **94**(14), 140412(2016).

27. Du, C. H., Wang, H. L., Yang, F. Y., Hammel, P. C. Systematic variation of spin-orbit coupling with d-orbital filling: Large inverse spin Hall effect in 3d transition metals. *Phys. Rev. B* **90**(14), 140407(2014).

28. Qu, D., Huang, S. Y., Chien, C. L. Inverse spin Hall effect in Cr: Independence of antiferromagnetic ordering. *Phys. Rev. B* **92**(2), 020418(2015).

29. Baltz, V., Manchon, A., Tsoi, M., Moriyama, T., Ono, T., Tserkovnyak, Y. Antiferromagnetic spintronics. *Rev. Mod. Phys.* **90**(1), 015005(2018).

30. Kondo, J. Anomalous Hall Effect and Magnetoresistance of Ferromagnetic Metals. *Progress of Theoretical Physics* **27**(4), 772-792(1962).

31. Gu, B., Ziman, T., Maekawa, S. Theory of the spin Hall effect, and its inverse, in a ferromagnetic metal near the Curie temperature. *Phys. Rev. B* **86**(24)**,** 241303(2012).

32. Okamoto, S., Egami, T., Nagaosa, N. Critical Spin Fluctuation Mechanism for the Spin Hall Effect. *Phys. Rev. Lett.* **123**(19)**,** 196603(2019).

33. Fang, C., Wan, C. H., Yang, B. S., Qin, J. Y., Tao, B. S., Wu, H., et al. Determination of spin relaxation times in heavy metals via second-harmonic spin injection magnetoresistance. *Phys. Rev. B* **96**(13)**,** 134421(2017).

34. Liu, L. Q., Chen, C. T., Sun, J. Z. Spin Hall effect tunnelling spectroscopy. *Nat. Phys.* **10**(8)**,** 561(2014).

35. Kittel, C. *Introduction to Solid State Physics* (John Wiley & Sons, Inc., 1967).

36. Sawabu, M., Ohashi, M., Ohashi, K., Miyagawa, M., Kubota, T., Takanashi, K. The electrical resistivity of epitaxially deposited chromium films. *J. Phys.: Conf. Ser.* **871**012002(2017).

37. Mattson, J., Brumitt, B., Brodsky, M. B., Ketterson, J. B. Magnetotransport studies of epitaxial Cr thin films. *J. Appl. Phys.* **67**(9)**,** 4889-4891(1990).

38. Jedema, F. J., Filip, A. T., van Wees, B. J. Electrical spin injection and accumulation at room temperature in an all-metal mesoscopic spin valve. *Nature* **410**(6826)**,** 345-348(2001).

39. Takahashi, S., Maekawa, S. Spin injection and detection in magnetic nanostructures. *Phys. Rev. B* **67**(5)**,** 052409(2003).

40. Bass, J., Pratt, W. P. Spin-diffusion lengths in metals and alloys, and spin-flipping at metal/metal interfaces: an experimentalist's critical review. *J. Phys. Condens. Matter.* **19**(18)**,** 183201(2007).

41. Yakata, S., Ando, Y., Miyazaki, T., Mizukami, S. Temperature dependences of spin-diffusion lengths of Cu and Ru layers. *Jpn. J. Appl. Phys., Part 1* **45**(5A)**,** 3892(2006).

42. Isasa, M., Villamor, E., Hueso, L. E., Gradhand, M., Casanova, F. Temperature dependence of spin diffusion length and spin Hall angle in Au and Pt. *Phys. Rev. B* **91**(1)**,** 024402(2015).

43. Parkin, S. S. P., Kaiser, C., Panchula, A., Rice, P. M., Hughes, B., Samant, M., et al. Giant tunnelling magnetoresistance at room temperature with MgO (100) tunnel barriers. *Nat. Mater.* **3**(12)**,** 862-867(2004).

44. Han, X., Wang, X., Wan, C., Yu, G., Lv, X. Spin-orbit torques: Materials, physics, and devices. *Appl. Phys. Lett.* **118**(12)**,** 120502(2021).

45. Onoda, S., Sugimoto, N., Nagaosa, N. Quantum transport theory of anomalous electric, thermoelectric, and thermal Hall effects in ferromagnets. *Phys. Rev. B* **77**(16)**,** 165103(2008).

46. Miyazaki, T., Tezuka, N. Giant magnetic tunneling effect in Fe/Al2O3/Fe junction. *J. Magn. Magn. Mater.* **139**(3)**,** L231(1995).

47. Bloch, F. For electric Resistance law at low Temperatures. *Z. Phys.* **59**(3-4)**,** 208-214(1930).

48. Ziman, J. M. *Electrons and Phonons: The Theory of Transport Phenomena in Solids*.(Oxford University Press: Oxford, 2001).

49. Baber, W. G. The contribution to the electrical resistance of metals from collisions between electrons. *Proc. R. Soc. A* **158**(A894)**,** 0383-0396(1937).

50. Wölfle, P. and Ziman, T. Theory of record thermopower near a finite temperature magnetic phase transition in IrMn. *Phys. Rev. B* **104**, 054441 (2021).

Methods

Sample Preparation

The single-crystal stacks are prepared in molecular beam epitaxial system with ultrahigh vacuum. Before deposition, the MgO(001) substrate was annealed at 700 °C for one hour to degas the surface, followed by depositing a 10 nm MgO seed layer at 450 °C to block the C impurity diffusion. The Cr layer was then deposited at 31 °C and followed by an in-situ post-annealing at 600 °C to obtain a flat Cr (001) surface. The temperature was maintained at 78 °C and 57 °C to deposit the MgO and Fe layers. A second post-annealing at 480 °C was performed to improve the crystalline quality of Fe. In the end, a 5 nm Au capping layer was deposited at 88 °C to prevent the surface oxidation. Surface structures of each stack were monitored by reflected high-energy electron diffraction (RHEED) throughout the growth process (Extended Data Fig. 1). After magnetism characterization with vibrating sample magnetometer (VSM), the sample is fabricated into tunnel junctions with standard ultraviolet lithography and ion-beam etching process. The junction is surrounded by oxide SiO_2 or Al_2O_3 to isolating top electrode and bottom electrodes.

Electrical measurement

For ISHE and DSHE measurement, ac current with low frequency is applied with Keithley 6221 and voltage is detected with lock-in amplifier SR830. The first harmonic and second harmonic signals are picked-up by two SR830 simultaneously. We use the frequency of 8.3 Hz and a preamplifier SR560 for good signal-to-noise ratio. The ISHE or DSHE signal in the manuscript is only first harmonic signals, which is disentangled with thermoelectric transport effects. The out-of-plane field gives an ordinary Hall signal, which changes linearly with the field magnitude (Extended Data Fig. 2). And the variation of magnitude of the small ac current we use between 10 µA to 70 µA does not affect the $R_{ISHE(DSHE)}$ value and could modified the signal-to-noise ratio (Extended Data Fig. 3). Magnetic field and temperature conditions are offered by QD PPMS. Samples are mounted on a sample holder with Al wire-bounding.

Theoretical consideration on the SHE by AFM spin fluctuation

Here, we briefly discuss how the formalisms derived in Ref. 32 for the FM spin

fluctuation should be modified when the AFM spin fluctuation is considered. The main difference from the FM fluctuation is that electrons at the Fermi surface are scattered by the AFM fluctuation with its spectral function given by

$$B_{\mathbf{q}}(\omega) = \frac{1}{\pi} \frac{\omega/\Gamma}{\{\delta + A(\mathbf{q} - \mathbf{Q})^2\}^2 + (\omega/\Gamma)^2}.$$

Here, δ measures the distance from the magnetic ordering as $\delta \propto T - T_N$ at $T > T_N$ and $\delta \propto M^2$ $T < T_N$ with M being the ordered moment, which behaves as $M \propto \sqrt{T_N - T}$ near T_N. A constant A is introduced so that $A(\mathbf{q} - \mathbf{Q})^2$ has the unit of energy, and Γ is the Landau damping. In contrast to the similar expression in Ref. 32, (i) the momentum dependence is given by $A(\mathbf{q} - \mathbf{Q})^2$ with $\mathbf{Q}$ the magnetic wave vector characterizing the magnetic ordering, and (ii) the damping term Γ is independent of momentum. Because of (i), electrons that contribute to the SHE have to satisfy the nesting condition, i.e., momenta $\mathbf{k}$ and $\mathbf{k} + \mathbf{Q}$ have to be on the Fermi surface. This difference may lead to the following modified forms:

$$\sigma_{SH}^{ss} \propto \tau^2 \, \delta \, I^2(T, \delta)$$

for the skew scattering contribution, and

$$\sigma_{SH}^{sj} \propto \tau \, \tilde{I}(T, \delta)$$

for the side jump contribution. As in Ref. 32, $I(T, \delta)$ is given by

$$I(T, \delta) = \frac{1}{(2\pi)^3} \int d^3p \frac{1}{\sinh(\hbar \mathbf{v}_F \cdot \mathbf{p}/T)} \frac{\hbar \mathbf{v}_F \cdot \mathbf{p}/\Gamma}{(\delta + Ap^2)^2 + (\hbar \mathbf{v}_F \cdot \mathbf{p}/\Gamma)^2},$$

where the momentum integral variable is changed from $\mathbf{q} - \mathbf{Q}$ to $\mathbf{p}$ by measuring it from the magnetic wave vector $\mathbf{Q}$, and $\mathbf{v}_F$ is the Fermi velocity. τ is the carrier lifetime, which is assumed to be independent of momentum that satisfies the nesting condition. $\tilde{I}(T, \delta)$ appearing in the expression of σ_{SH}^{sj} is given by

$$\tilde{I}(T, \delta) = \frac{1}{(2\pi)^3} \int d^3p \int d\omega \frac{1}{\sinh(\omega/T)} \frac{\omega/\Gamma}{(\delta + Ap^2)^2 + (\omega/\Gamma)^2}.$$

A similar expression is derived for the electron self-energy by the AFM spin fluctuation in Ref. 50 (Wölfle and Ziman Phys. Rev. B **104**, 054441 (2021)). Except for the vicinity of the magnetic transition temperature T_N, $I(T, \delta)$ and $\tilde{I}(T, \delta)$ behave as $I(T, \delta) \approx T^3/\delta$ and $\tilde{I}(T, \delta) \approx T^2/\sqrt{\delta}$, respectively. Thus, σ_{SH}^{ss} and σ_{SH}^{sj} behave as

$$\sigma_{SH}^{ss} \propto \tau^2 \, T^6/\delta$$

and

$$\sigma_{SH}^{sj} \propto \tau \, T^2/\sqrt{\delta},$$

respectively. As shown in Fig. 2d, the resistivity shows a smooth crossover behavior from $\rho \sim const. + \alpha T^2$, where α is a constant, at low temperatures (Extended Data Fig. 5a) to $\rho \propto T$ at high temperatures. Thus, the carrier lifetime is dominated by the impurity or disorder and the electron-electron interaction at low temperatures and by the phonon scattering at high temperatures. Assuming that δ remains constant away from T_N and $\tau \propto \sigma \sim 1/\rho$, one finds

$$\sigma_{SH}^{ss}/\sigma^2 \propto \, T^6$$

and

$$\sigma_{SH}^{sj}/\sigma^2 \propto \, T^2 + \alpha T^4.$$

Lorraine and Grand Nancy.

Author contributions

C. F. and C. W. conceived and designed the experiment. S. O. and N. N. provided the theoretical analysis. Y. L., X. Z., T. M. and J. Q. grew the single crystal films. C. F., X. W., C. G. and J. D. carried out the VSM and TEM characterization. C. F. and C. W. fabricated the devices and conducted the electrical measurement. G. Y., Z. W., N. T., S. S. P. P. and N. N. gave suggestions on the experiments. Y. L., X. H. supervised this study. All authors discussed the results and prepared the manuscript.

Competing interests

The authors declare no competing interests.

Figure

a
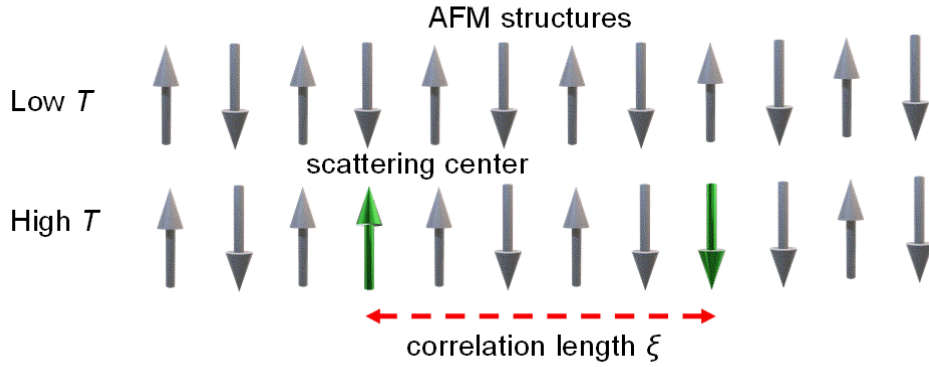
b
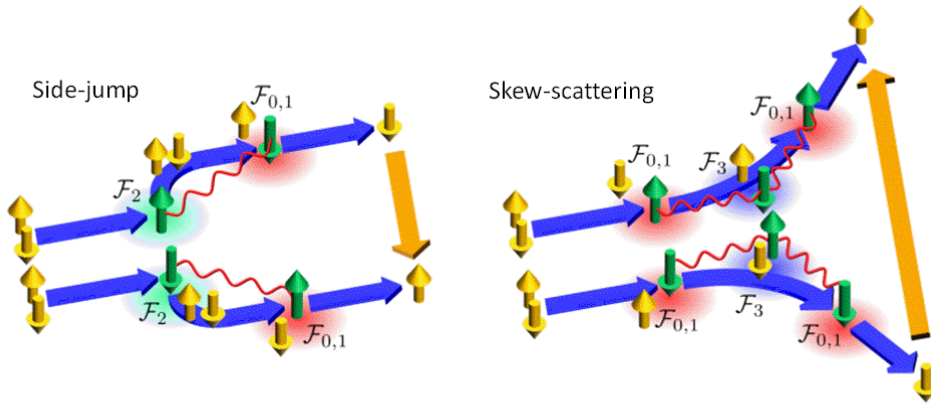
Fig. 1 | Fluctuation Spin Hall effect. a, Correlation length ξ of antiferromagnetic materials. The grey arrows are the magnetic spins forming the AFM order. Green arrows act as the scattering centers activated by spin fluctuation. The ξ represents the correlation length within which the scattering centers can antiparallelly correlate with each other. The ξ becomes divergent with T approaching T_N from low temperatures. **b,** Antiferromagnetic spin fluctuation. Spin current (orange allows) is caused by AFM spin fluctuation. Yellow arrows are conduction electron spins, and green arrows are local spins. In the $\mathcal{F}_{2(3)}$ scattering processes, the deflected direction of scattered electrons depends on the direction of the local spins (the conductive electron spins), combining $\mathcal{F}_{0,1}$ to form the side-jump-type (skew-scattering-type) contribution to σ_{SH}. The red wavy curves represent the propagators of AFM spin fluctuation, which relates to the correlation length.
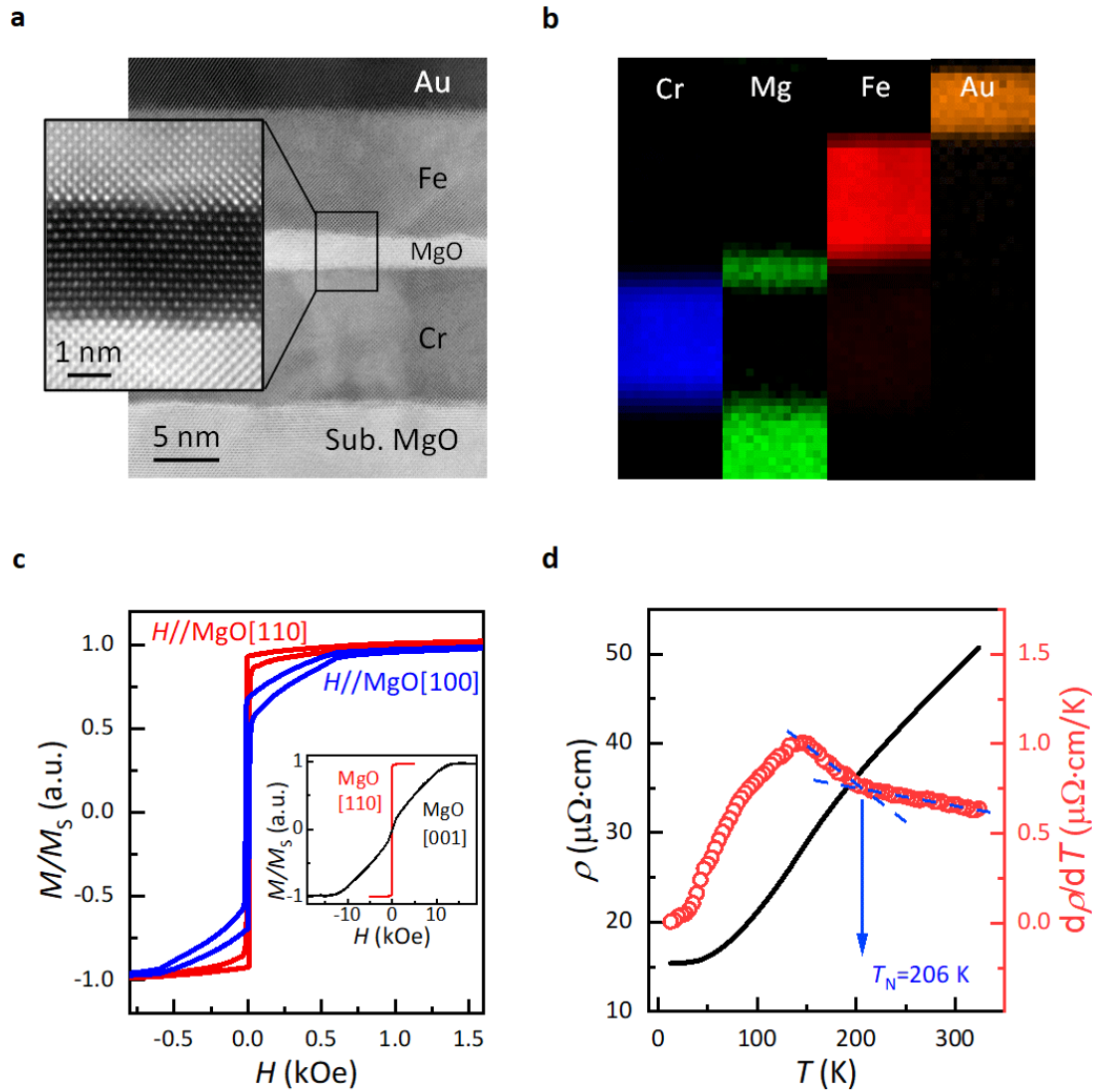
Fig. 2 | Magnetic tunnel junction Cr/MgO/Fe/Au stacks. a, High resolution cross-sectional transmission electron microscope (HRXTEM) pattern of the junction. Flat interfaces are indicated. Inset: Black field image of the region near MgO barrier. Epitaxy relation was well defined globally throughout the sample. Cr and Fe lattices grew along the MgO [001] direction. **b,** The electron energy loss spectroscopic (EELS) mapping of the Cr, Fe, Mg and Au elements. **c,** Magnetic hysteresis loop of MTJ films with external magnetic field along MgO [110] (red, also noted as in-plane) and MgO [100] (blue). Inset: MgO [001] (black, also noted as out-of-plane) and reproduction of MgO [110] to show the in-plane easy axis of Fe layer. **d,** The temperature dependence of resistivity (black line) and its differential with respect of T (red circles) in 10 nm Cr.
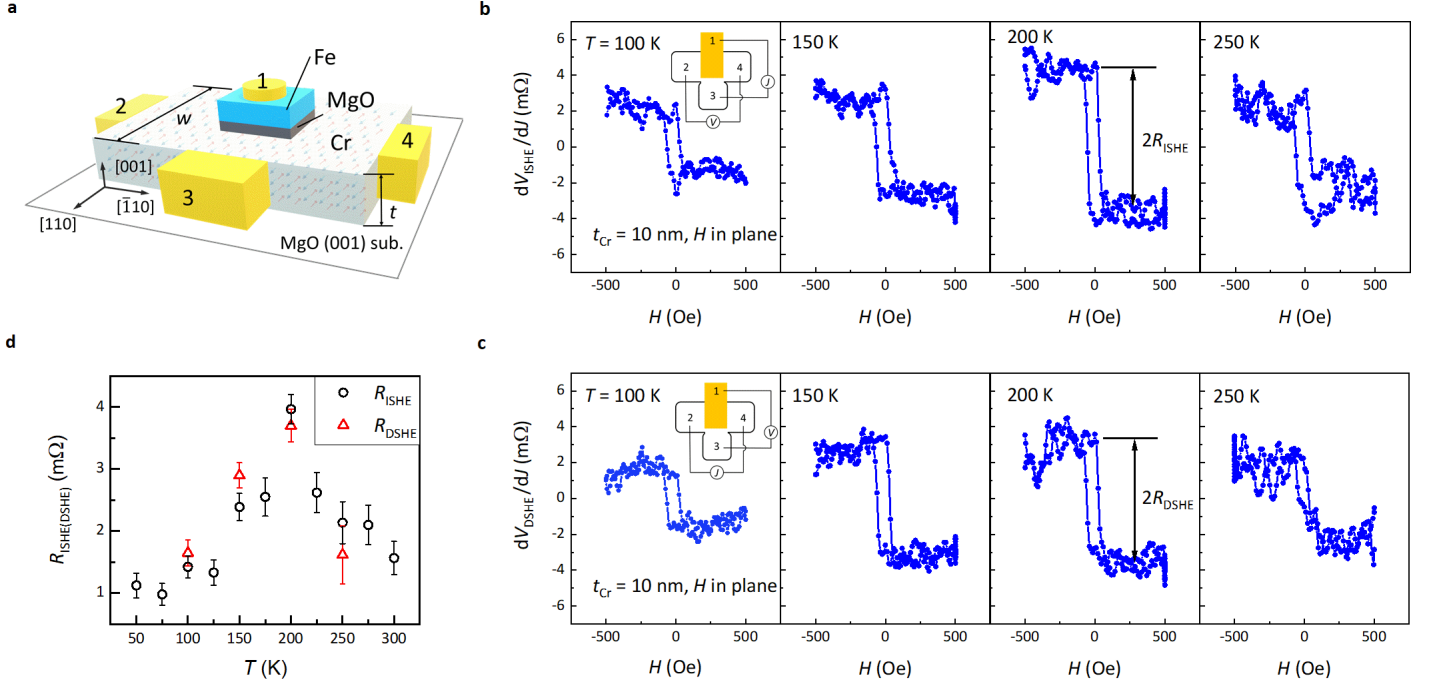
Fig. 3 | Detection of SFHE with ISHE and DSHE set-up. a, Device schematic diagram of fabricated MTJ devices. **b,** ISHE and **c,** DSHE in 10 nm Cr with in-plane magnetic field along MgO [110] at different temperatures. Inset: Measurement schematic diagram of ISHE with current J loaded between electrode 1 and 3 and V_{ISHE} collected between electrode 2 and 4 and DSHE with exchanging the source and measure meters. Both ISHE and resistance was observed when **H** was applied in in-plane (blue) and vanished when **H** was out-of-plane applied (Extended Data Fig. 2). $R_{ISHE(DSHE)}$ represented the saturated value of $dV_{ISHE(DSHE)}/dJ$. **d,** Critical spin fluctuation enhanced R_{ISHE} (black circles) and R_{DSHE} (red squares) resistance in MTJ device. The magnitude of $2R_{ISHE(DSHE)}$ is given by the difference between intercepts of linear fitting of two resistance platform and the error bar is given by the standard error of the linear fitting.
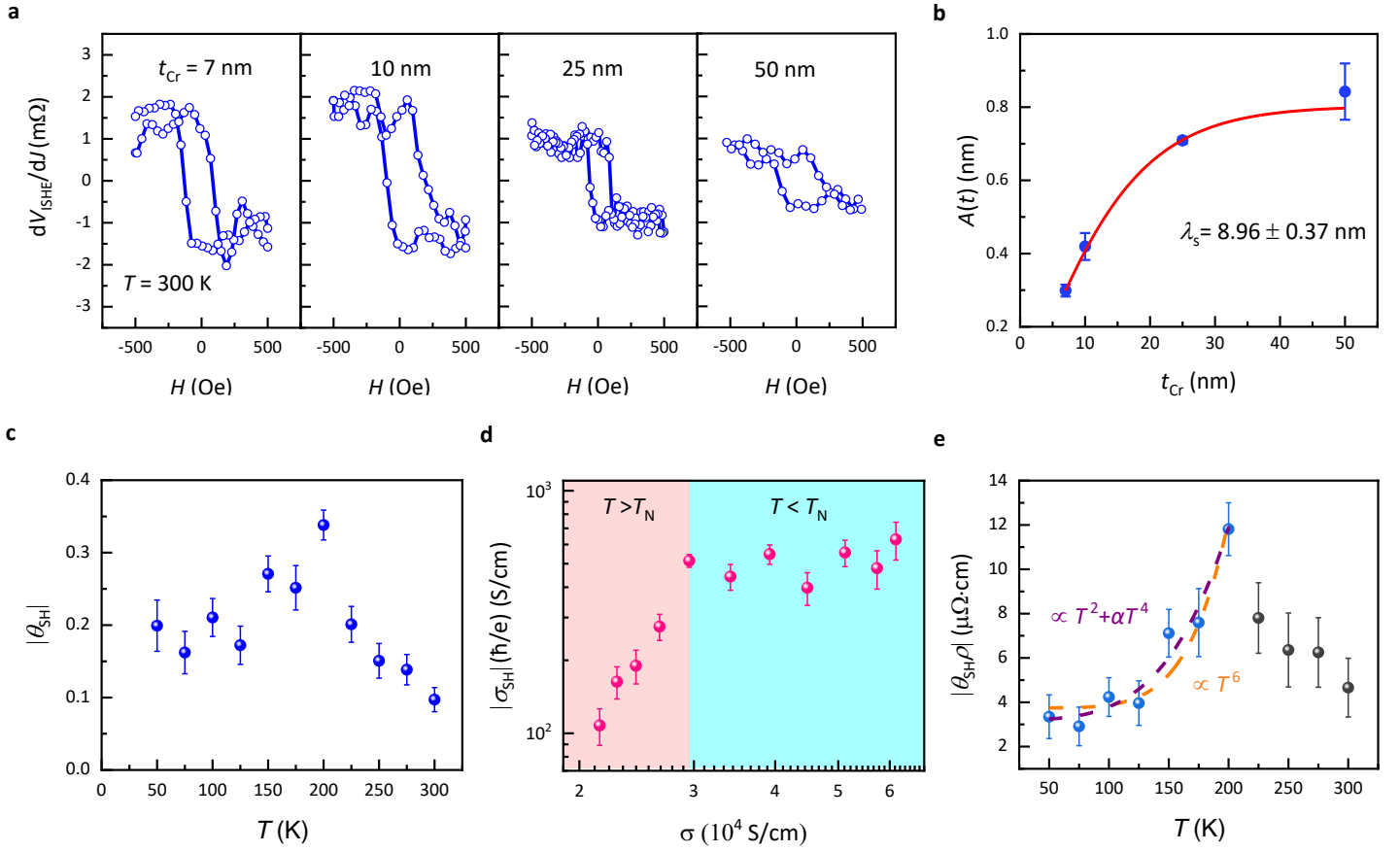
Fig. 4 | Spin transport properties in Cr. a, ISHE resistance in Cr at 300 K with different thicknesses. **b,** Thickness dependence of the factor $A(t)$. Red line is the fitting result following Equation (2). **c,** Temperature dependence of SHA. **d,** Scaling relation between conductivity and spin Hall conductivity. **e,** Temperature dependence of product of SHA and resistivity. Orange dash line shows the fitting result of $\sigma_{SH}^{sj}/\sigma^2 \propto T^2 + \alpha T^4$ with the adjusted R^2 (coefficient of determination) = 0.95. Purple dash line shows the fitting result of the $\sigma_{SH}^{ss}/\sigma^2 \propto T^6$ with the adjusted $R^2 = 0.89$.
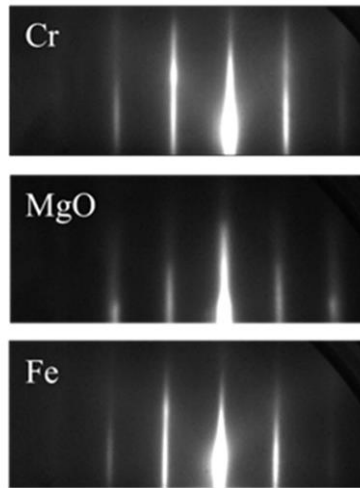
Extended Data Fig. 1| RHEED pattern of MTJ film. RHEED pattern of the annealed Cr, MgO and Fe layers further confirmed the epitaxial growth mode. The sharp streaky patterns indicate a high-quality epitaxial growth character of our sample.
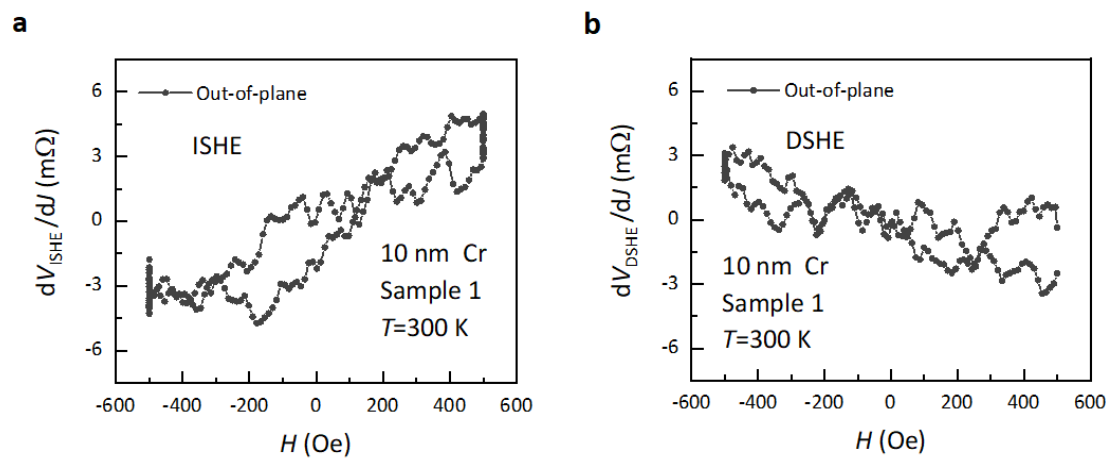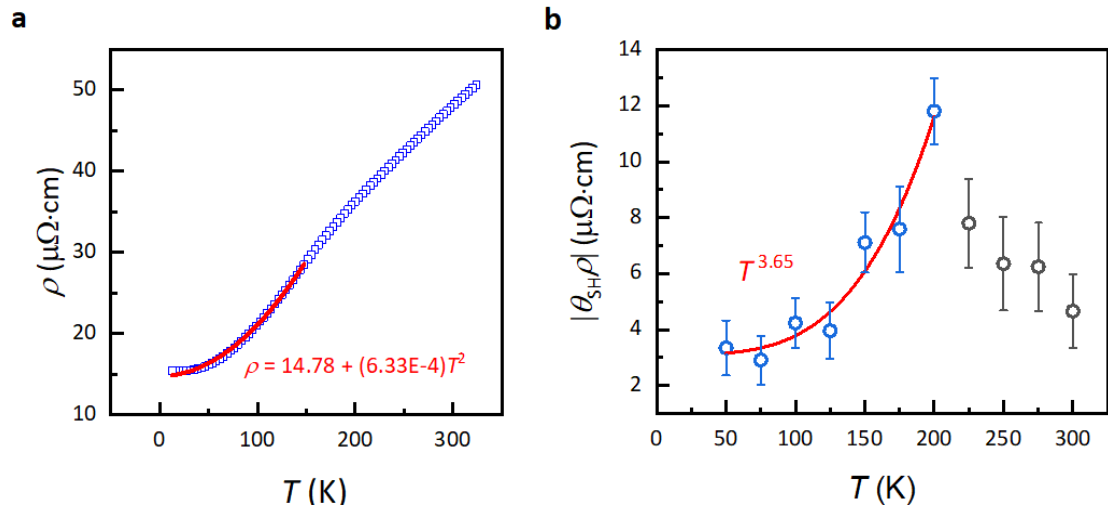

Extended Data Fig. 2| Spin Hall signal with out-of-plane magnetic field H. a, ISHE. **b,** DSHE
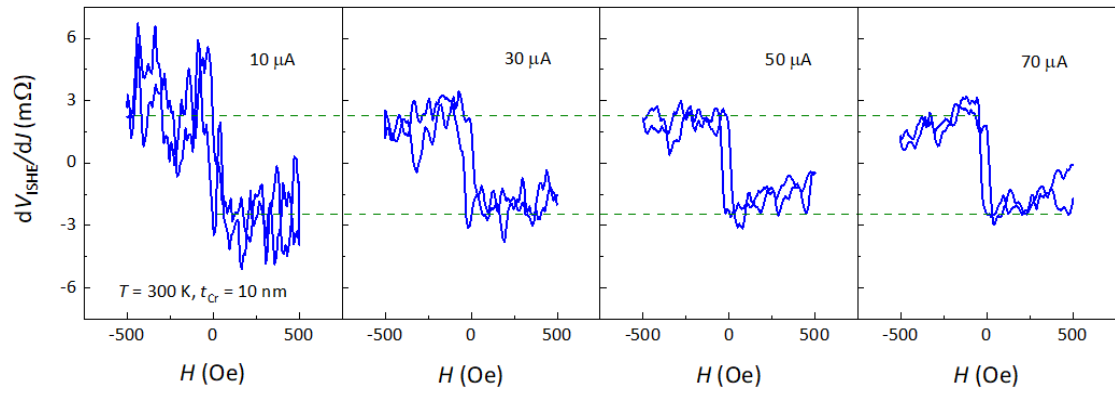
Extended Data Fig. 3 | Spin Hall signal with different magnitude of injection current
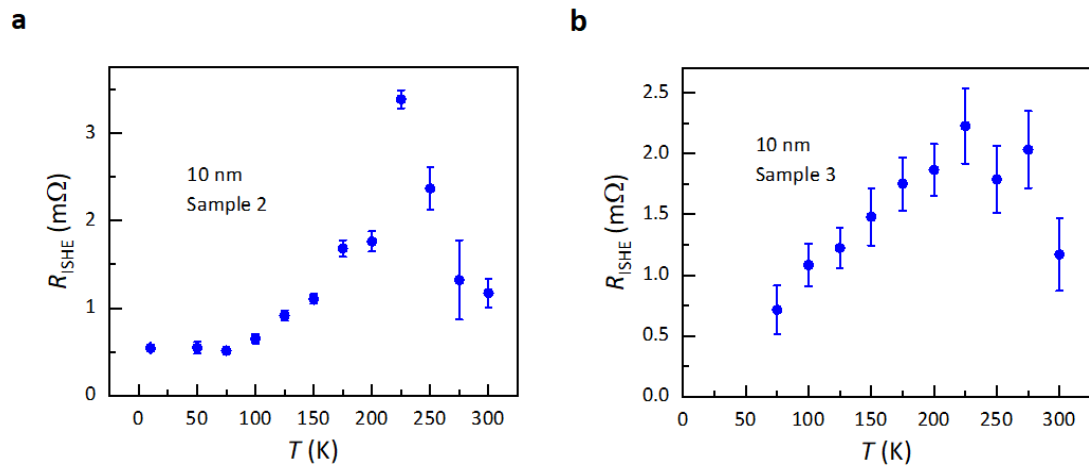
Extended Data Fig. 4 | Inverse Spin Hall signal in more samples. a, Sample 2. **b,** Sample 3.

Extended Data Fig. 5 | Fitting of T-dependence of resistivity and spin resistivity. a, Resistivity fitting. Data points with the square shape are repeat of ones in Fig. 2d. Fitting $\rho \sim const. + \alpha T^2$ gives the α. **b,** Spin resistivity fitting. Data points with the circle shape are repeat of ones in Fig. 4e. Red line indicates a power-law fitting of the spin Hall resistivity at and below 200 K.